This document is confidential and is proprietary to the American Chemical Society and its authors. Do not copy or disclose without written permission. If you have received this item in error, notify the sender and delete all copies.

# Complex Spherical Phases in a Zwitterion-tethered Diblock Copolymer Melt

Journal:	Macromolecules			
Manuscript ID	ma-2023-008469.R2			
Manuscript Type:	Article			
Date Submitted by the Author:	n/a			
Complete List of Authors:	Grim, Bradley; Arizona State University, Chemical Engineering Beyer, Frederick; U.S. Army Research Laboratory, Green, Matthew; Arizona State University, Chemical Engineering			

SCHOLARONE™ Manuscripts

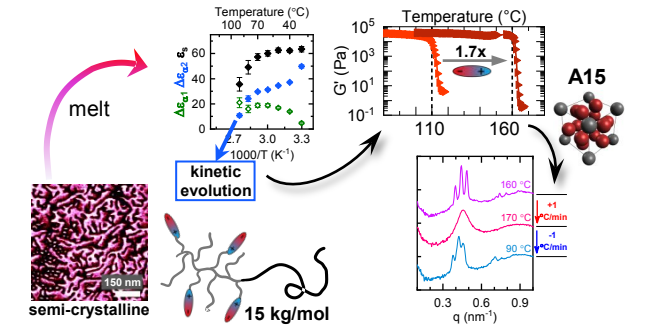
# Complex Spherical Phases in a Zwitterion-tethered Diblock Copolymer Melt

Bradley Grim<sup>1</sup>, Frederick L. Beyer<sup>2</sup>, Matthew D. Green<sup>1,\*</sup>

<sup>1</sup>Chemical Engineering, School for Engineering of Matter, Transport and Energy, Arizona State University, Tempe, AZ 85287, USA

<sup>2</sup>U.S. Army Research Laboratory, Aberdeen Proving Ground, MD 21005, USA

# For Table of Contents use only



**KEYWORDS:** Frank-Kasper A15 phase, block polymer, zwitterion, self-assembly

ABSTRACT: The recent surge of work expanding our understanding of complex spherical packing in block polymers (BPs) has unlocked new design space for the development of advanced soft materials. The continuous matrix phase which percolates throughout spherical morphologies is ideal for many applications involving transport of ions or other small molecules. Thus, determining the accessible parameter range of such morphologies is desirable. Bulk zwitterion-containing BPs hold great potential within the realm of electroactive materials while remaining relatively untapped. In this work, three architecturally and compositionally asymmetric diblock polymers were prepared with the majority block having zwitterions tethered to side chain termini at different ratios. The A15 Frank-Kasper phase was observed in two samples (~ 15 kDa),

<sup>\*</sup>Corresponding author: mdgreen8@asu.edu

separated by a substantially higher  $T_{ODT}$  after increasing zwitterion content 1.7-fold. For the highest zwitterion content sample, phase transitioning out of the kinetically trapped, liquid-like packing (LLP) state was found to correlate to a decline in the dielectric strength of zwitterionic relaxation processes which suggests zwitterionic interactions to be governing the phase transition kinetics. Upon slowly cooling from the disordered state, Frank-Kasper phases reappeared with signs of kinetic arrest.

## INTRODUCTION

Our understanding of block polymer (BP) thermodynamics has progressed substantially alongside advancements in the underlying theoretical models. <sup>1–15</sup> Relative to the simplified instance of linear diblock copolymer self-assembly, <sup>12,16</sup> several thermodynamic driving forces have the ability to shift, deflect, flip, and unveil transition boundaries in unique fashions. <sup>17–32</sup> The list of modifying parameters is extensive, and each addition couples a new dimension to the phase space. While there is still much to learn about BP self-assembly, this cornucopia of factors provides a vast and broadening landscape of exciting opportunities for soft material design. <sup>33–43</sup>

In block copolymer melts, the Flory-Huggins interaction parameter ( $\chi$ ) and the total number of repeat units (N) dictate the segregation strength between blocks which form ordered morphologies at sufficiently large  $\chi N$ .<sup>12,16</sup> At constant  $\chi N$ , the geometry of the interface dividing phase separated blocks is subject to a competition between chain stretching penalties of the respective blocks.<sup>44</sup> Two factors which lead to disparate chain stretching energies between blocks are compositional asymmetry and conformational asymmetry with the latter describing blocks as having unequal statistical segment lengths (b).<sup>45</sup> Just as compositional asymmetry will favor curvature of the interface towards the volumetric minority block, conformational asymmetry will favor curvature towards the block with greater b. Hence, constructively tuning these asymmetric parameters can have a profound impact on the stabilization of

spherical phases.<sup>45–49</sup> At sufficiently high degrees of conformational asymmetry, complex interfacial geometries are stabilized which can give rise to new spherical morphologies exhibiting topological close packing (TCP) such as Frank-Kasper (FK) phases.<sup>29,50–53</sup>

Prediction of A15 phase stability by Grason at al. in  $2003^{29}$  followed by discovery of the  $\sigma$  phase by Lee et al. in 2010<sup>54</sup> for BPs sparked a surge of papers on the topic over recent years.<sup>55,56</sup> Conformational asymmetry plays a paramount role in stabilizing these complex, low symmetry spherical morphologies.<sup>53</sup> Differing polymer chemistries offer a small range of statistical segment lengths, but rarely with a large enough difference to afford complex spherical phases. Linear, diblock copolymers (dBPs) with hard and elastic blocks can form FK phases, 51,54,57-62 but often require rapid cooling from the disordered state to kinetically seed FK formation over other classic morphologies. Some methods for bypassing these processing requirements are mixing with homopolymers<sup>63-67</sup> and BP blending.<sup>51,68-72</sup> Additionally, architectural alterations such as branching or grafting can decrease b, thereby increasing conformational asymmetry without having to drastically alter polymer chemistry. BP branching or grafting alterations includes dendritic, 29,73 bottlebrush or comb-like, 74-78 and miktoarm topologies, 24,50,77,79-81 which have all demonstrated a profound stabilization of sphere-forming regions. Reports on BPs exhibiting FK phases have also been somewhat limited to low molecular weights, <10 kDa, due to kinetic chain transfer limitations between micelles at higher molecular weights, 82 although some exceptions have been revealed including bidisperse dBP blending, 68,70 BP/homopolymer blending, 63 multiblock, miktoarm, and star architectures, 58,79,83 and extensive grafting. 76

The addition of ionic species into BPs can endow the material with electrochemical properties. Zwitterions constitute a covalently tethered pair of ions which can drastically increase the dielectric constant of soft materials, <sup>84</sup> in turn contributing to increased electrolytic performance. <sup>85–87</sup> Most electrolytic applications benefit from having a continuous ionic domain such as that found in spherical morphologies. <sup>88,89</sup> Thus, it is important to understand how to expand and where to target the phase space of continuous phases in ion-containing BPs. FK and other spherical phases consume a very small portion of

the phase space, making them a difficult target to hit, especially when convoluted by electrostatic interactions. In addition to conformational asymmetry, electrostatic interactions are capable of radically altering the shape and location of transition boundaries within the BP phase diagram. <sup>19,22,23,33,42,90,91</sup> This factor may be influencing the continued scarcity of ion-containing BPs which display complex spherical packing. <sup>88,89,92–94</sup> In one instance, Xie et al. observed a C15 Laves phase over a narrow compositional window in a ternary blend of polystyrene (PS), poly(ethylene oxide) (PEO), and PS-*b*-PEO doped with lithium salts ([Li<sup>+</sup>]/[EO] = 0.06). <sup>93</sup> In another instance, Park and coworkers observed the A15 phase with an ion-rich matrix in a few low molecular weight, acid-tethered polystyrene-b-poly(methylbutylene) *d*BPs doped with ionic liquids. <sup>88,89,94</sup> Samples which conformed to the A15 phase exhibited superior ion transport efficiency over those with LAM, HEX, and even BCC morphologies. The qualitative reasoning behind Park's findings inferred greater electrostatic interactions at the interface to be stabilizing the A15 micelles by promoting backbone collapse within the charged phase, thus reducing its statistical segment length (*b*). <sup>95</sup>

In the present work, complex spherical packing in compositionally and architecturally asymmetric, zwitterion-tethered diblock polymer melts are reported with emphasis on the role of zwitterionic interactions within this realm. The polymer system contains an invariant degree of polymerization with nominal changes to molecular weight and dispersity between samples and was designed to isolate the effects of zwitterion content on the overall phase behavior. The dynamic phase behavior of solvent cast, bulk films were explored using small-angle X-ray scattering (SAXS), rheology, atomic force microscopy (AFM), and dielectric relaxation spectroscopy (DRS) to understand the role zwitterions play in this complex self-assembly.

#### **EXPERIMENTAL SECTION**

**Materials.** Ultra-high purity nitrogen (99.999%) was used for all syntheses and material storage. Poly(ethylene glycol) methyl ether (mPEG, 5 kg/mol), Butanethiol (BuSH, 99%), dimethylamino ethanethiol hydrochloride (DMAET-HCl, 95%), 2,2-dimethoxy-2-phenylacetophenone (DMPA, 99%), 1,3-propanesultone, and dry dimethylformamide (DMF, 99.5%) were obtained from Sigma-Aldrich and

used as is unless otherwise specified. Ultrapure water (upH2O) was obtained from a Milli-Q Advantage 10 purification system. Methanol (ACS grade) and chloroform (ACS grade) were used as is. Tetrahydrofuran (THF, HPLC grade) was purged with nitrogen for 30 mins and ran through alumina columns using an MBraun solvent system prior to use in anionic polymerization. Allyl glycidyl ether (AGE,  $\geq$  99%) was obtained from Sigma-Aldrich and dried by stirring over solid butyl magnesium chloride in vacuo for 30 minutes, distilled at 60 °C into a liquid nitrogen chilled monomer burette, degassed by 3 freeze-pump-thaw cycles, and stored under nitrogen at -5 °C until use. Naphthalene was recrystallized in diethyl ether (3x) and stored in a desiccator until use. Potassium naphthalenide solutions were prepared under nitrogen by mixing potassium metal and 1.1 eq. naphthalene in THF overnight in a sealed graduated cylinder custom fitted with a 4 mm PTFE stopcock.

Molecular Characterizations. Dispersity (*D*) of PEO-*b*-PAGE was calculated from the differential refractive index (dRI) relative to PS standards at 40 °C in THF by gel permeation chromatography (GPC) using a Waters e2695 separations module attached to an Optilab T-rEX refractive index detector. The concentration of sample was 5 mg/mL in THF with a 1 mL/min elution rate. Thermal transitions were determined by differential scanning calorimetry (DSC) using a TA Instruments Q1000 with refrigerated cooling. Tzero aluminum pans were hermetically sealed with 5-10 mg of dry sample and kept under a continuous flow of nitrogen throughout the experiment. DSC experiments involved heating to 110 °C for 10 min, cooling at 5 °C/min to -90 °C, held for 10 min, and heating at 10 °C/min to 150 °C. Number average molecular weight (M<sub>n</sub>) and composition were determined via ¹H-NMR using a 500 MHz Bruker instrument and a sample concentration of 15 mg/mL in CDCl<sub>3</sub> with 0.3% TMS. M<sub>n</sub> for PEO macroinitiators (mPEG) was determined using end-group analysis via terminal CH<sub>2</sub> groups, noting that use of the terminal CH<sub>3</sub> group resulted in a nearly 2 kDa overestimate of the molecular weight. Composition of PEO-*b*-PAGE was calculated using the integral ratio between ethylene oxide and AGE monomers. Zwitterion fraction ([SB]/[AGE]) was calculated by the integral ratio between butyl and dimethylamine moieties along the PAGE block prior to the synthetic step producing the SB zwitterion.

Scheme 1. Synthetic scheme of diblock polymers studied, including sample nomenclature and compositional definition for SB content.

**Table 1.** Characteristics and compositions of the parent PEO-PAGE and subsequent functionalized diblock polymers.

Name	$N_{EO} \atop a$	$N_{AGE}$	<i>Y</i> % <sup>b</sup> (mol%)	$M_{n,total}^{c}$ (kg/mol)	$wt_{PEO}^{d}$	$M_{w}/M_{n}$
PEO-PAGE	113	47.1	-	10.4	0.48	1.27
SB5	113	47.1	4.9	14.8	0.33	-
SB10	113	47.1	10.0	15.1	0.32	-
SB17	113	47.1	17.4	15.6	0.31	-

<sup>a</sup> Degree of polymerization (N) of ethylene oxide (EO) and allyl glycidyl ether (AGE) within the parent PEO-PAGE BP were determined using <sup>1</sup>H NMR. <sup>b</sup> The mol% of sulfobetaine (SB) within the PAGE block (Y%) was calculated using <sup>1</sup>H NMR based on the integral ratios between butyl and dimethylamine groups resulting from thiol-ene "click" reactions (Figure S1) and assumed to be unchanged after production of the SB moiety in the final reaction step (Scheme 1). <sup>c</sup> Total number-average molecular weights ( $M_{n,total}$ ) were calculated based on previously obtained molar compositions of individual monomers. <sup>d</sup>  $wt_{PEO}$  defines the weight fraction of PEO within each BP. <sup>e</sup> Molecular weight dispersity ( $M_w/M_n$ ) of PEO-PAGE was determined using GPC and was assumed similar to that of the functionalized BPs given the mild conditions chosen for thiol-ene "click" reactions.

Synthesis of poly(ethylene oxide-*b*-allyl glycidyl ether) (PEO-PAGE). Anionic ring-opening polymerizations were performed using well-established protocol for polyether extension from hydroxyl functionalities<sup>96–100</sup> and carried out using standard high vacuum techniques for anionic polymerization.<sup>101–103</sup> Reactions were conducted under ultra-high purity nitrogen using a Schlenk line fixed to a custom thick-

walled borosilicate reactor fitted with #7 and #15 ACE-Threds for the septum and auxiliary glassware, respectively. All glassware was flame dried under high vacuum and tested for leaks immediately prior to use. Bulk PEO macroinitiator was added to the reactor and held under high vacuum at 100 °C overnight to remove any moisture contained within it. After cooling the reactor to 40 °C, THF was introduced under inert conditions and the solution was stirred until complete dissolution of the PEO. After cooling the reactor to room temperature, potassium naphthalenide in THF (2 M) was slowly titrated into the stirring reactor via cannula transfer until a light yellowish green color persisted for 30 min. Purified AGE was then added to the reaction and stirred at 50 °C for 3 days. The final reaction concentration was 36 wt% reagents in THF. Polymerization was terminated using degassed acidic methanol, the polymer was precipitated in n-hexane, and the precipitate was dried under vacuum overnight. A labelled ¹H-NMR spectrum can be found in Figure S1.

Functionalization of PEO-PAGE. An example thiol-ene "click" reaction proceeds as: 3 g PEO-b-PAGE (1 eq. allyl) was dissolved in 100 mL methanol with 0.1 eq. DMPA and 8 eq. thiol reagents at the desired ratios (BuSH:DMAET-HCl) in a 200 mL round bottom flask equipped with a magnetic stir bar. The reaction flask was sealed with a rubber septum, purged with nitrogen for 30 min, and then stirred while being irradiated with 365 nm UV light (8 W) for 1.5 h. The solution was vacuum dried using a rotary evaporator to remove most of the solvent and BuSH. Neutralization of the HCl and polymer purification were performed simultaneously in the following liquid-liquid extraction. The functional polymer and remaining salts were removed from the flask using minimal amounts of chloroform and upH<sub>2</sub>O. Both mixtures were added to a 500 mL separatory funnel containing 100 mL chloroform and 300 mL upH<sub>2</sub>O with 2 eq. KOH relative to DMAET-HCl. After gentle agitation, the organic phase was removed, and the aqueous phase was extracted 2-3x with 50 mL chloroform. The organic phase was washed 4x with 200 mL upH<sub>2</sub>O with 1 eq. KOH relative to backbone amines, and then again very gently 4x with 200 mL upH<sub>2</sub>O. Finally, the organic phase was concentrated, precipitated into 300 mL cold diethyl ether, isolated via centrifugation (5000 rpm for 5 min), and dried overnight at 60 °C under dynamic vacuum. Finally, the ring-opening

reaction of 1,3-propanesultone to produce the sulfobetaine (SB) zwitterion<sup>104</sup> was performed by magnetically stirring the dry, dimethylamine (DMA)-functional BP and 1,3-propanesultone (1.1 eq. to DMA) together in dry DMF at 20 wt% reagents. The reaction flask was then sealed with a rubber septum and stirred at 60 °C for 24 h. The product was precipitated in diethyl ether and dried under vacuum overnight. Labelled <sup>1</sup>H-NMR spectra are provided in Figure S1.

Film preparation. Zwitterion-functional BPs were dissolved in DMF at 20 wt% and filtered through 3  $\mu$ m glass fiber syringe filters before casting into polished PTFE trays with rounded edges to make film removal easier. The solvent was evaporated at 50 °C for  $\geq$  2 days and the films were subsequently annealed and dried at 60-70 °C under dynamic vacuum for 4 days resulting in films  $\approx$  1 mm thick. None of the samples became semi-crystalline until all solvent was completely removed. Films were then removed from the vacuum oven and stored at room temperature under nitrogen, vacuum, or active desiccant until further testing.

**Rheology.** Rheological measurements were conducted using a Discovery HR-20 and/or Discovery HR-30 rheometer fixed with a 25 mm parallel plate geometry. Rotational mapping was calibrated using 3-8 precision cycles. Thick films ( $\approx 1$  mm) were quickly transferred into the environmental test chamber (ETC) and purged with nitrogen to minimize water absorption from ambient air before heating above  $T_{m,PEO}$  where the gap was then set to  $\approx 1$  mm using axial force to determine connection between the upper geometry and the sample. The sample edges were then trimmed, followed by a visual observation to confirm the absence of air bubbles. All isochronal temperature ramps were performed at 1 rad/s. Strain amplitude sweeps were performed to verify linear viscoelasticity at both the lowest and highest temperatures studied for each sample wherein the lowest strain within the linear regime was utilized. Isothermal frequency sweeps were conducted from 0.2-100 rad/s with a 10 min soak time at each temperature prior to measurement.

**Small-Angle X-ray Scattering (SAXS).** SAXS data were collected using a Xenocs "Xeuss 3.0 HR" camera with 8.04 keV photons generated by a Rigaku MicroMax-007HF rotating anode X-ray generator. The photons were collimated using a focusing optic and two scatterless slit apertures, producing a well-aligned

incident beam with wavelength ( $\lambda$ ) of 0.15418 nm. Data were collected using a Dectris Pilatus3R 300k solid-state detector at a sample-to-detector distance of 1.8 m. Two-dimensional data were azimuthally averaged to generate one-dimensional data, I(q), for analysis, where q is the magnitude of the scattering vector,  $q = 4\pi \cdot \sin(\theta)/\lambda$ , and  $2\theta$  is the scattering angle. The instrument configuration was calibrated using silver behenate. Intensity was placed on an absolute scale where feasible by normalizing the measured data by transmitted flux. This process was verified using a glassy carbon standard calibrated at the Argonne National Laboratory Advanced Photon Source. Data processing and analysis were performed using Wavemetrics Igor Pro v8 and procedures available for download from Argonne National Laboratory.  $^{105,106}$ 

The SAXS measurements with *in situ* heating and cooling, samples were placed in "sandwich cells" in which the sample is held between thin mica windows separated by a Viton<sup>TM</sup> o-ring, accommodating a sample approximately 1 mm thick. The sandwich cells were mounted on the heating block of a Linkam HFSX350-CAP heating stage. The samples were heated to target temperatures at a rate of 1 °C/min and held for 10 min prior to each measurement. Four successive measurements were taken at 5 min each and averaged, resulting in a total beam exposure time of 20 mins at each temperature. For cooling measurements, after the highest temperature in the heating profile was reached and data collected, the samples were cooled immediately at 1 °C/min to 90 °C. The samples were then held at 90 °C while successive 5 min data frames were collected.

Atomic Force Microscopy (AFM). AFM samples were derived from bulk films by cryo-microtoming a smooth surface on inner sections of cut pieces. The instrument used for surface smoothing was a Leica EM UC-7 Cryo-Ultramicrotome at a temperature of -40 °C. AFM imaging of those smoothed surfaces was performed on a Bruker MultiMode 8-HR using an ACSTA-10 probe from AppNano. Images were captured with 512 x 512 resolution at a scan rate of 1 Hz. Integral and proportional gains were set to 1.4 and 5.0, respectively. The amplitude setpoint ranged from 400 mV for SB5 to 500 mV for SB17 while the drive amplitude was maintained close to 50 mV for all samples.

Dielectric Relaxation Spectroscopy (DRS). Measurements were performed using a Solartron 1260 Impedance/Gain-Phase Analyzer with a Solartron 1296A Dielectric Interface to extend impedance measurements capabilities of the instrument. The sample cell was a DHR rheometer accessory made by TA Instruments which utilized the rheometer's ETC to provide temperature control and a continuous dry nitrogen atmosphere for the electrode cell. The 25 mm diameter electrodes provided were made from stainless steel and polished to a flat, mirror finish. Sample cells were first prepared by drying the electrodes at 120 °C for 1 h within the ETC, followed by an immediate transfer of thin bulk films from a dry environment onto the electrode surface. The sample was then enclosed in the ETC, purged, and further dried under constant nitrogen flow at 120 °C for 1 h to remove any remaining moisture. The upper geometry was then slowly pressed onto the material to a gap of 100  $\mu$ m. Equilibrium was determined based on three consecutive runs having perfectly overlapping  $\tan(\delta) = \varepsilon''/\varepsilon'$  traces. Any data which fell beyond the instrument limitations were masked from analysis. Such data was evidenced by an increase in real permittivity ( $\varepsilon'$ ) with increasing frequency (generally >1 MHz) as  $\varepsilon'$  should monotonically increase with decreasing frequency.

#### **RESULTS AND DISCUSSION**

## **Synthesis**

The polymers under investigation were constructed from a poly(ethylene oxide)-*b*-poly(allyl glycidyl ether) (PEO-*b*-PAGE) platform synthesized by anionic chain extension from a PEO macroinitiator. Allylic constituents along the PAGE block can be easily modified using thiol-ene "click" chemistry,<sup>107</sup> enabling one to tune architectural and compositional properties in parallel by choice of thiol (-SH) reagents. As illustrated in Scheme 1, allylic side chains were extended and charge fraction was tuned simultaneously by varying the ratio of thiol reagents (BuSH:DMAET-HCl) within the "click" reactions, which were performed at dilute BP concentrations (< 5 wt%) in methanol with an 8x excess of thiol reagents relative to allyls to

minimize cross-linking. A prior study by Barteau et al. performed similar photoinitiated thiol-ene reactions on PAGE homopolymers at concentrations of 30 wt% PAGE and 5-6x excess of thiol reagents relative to allyls and found no observable cross-linking in subsequent GPC traces.<sup>99</sup> With reaction conditions in the current study being significantly milder and more dilute, we assume cross-linking to be negligible.

Thorough purification of thiol reagents and any excess salts is deemed necessary, especially within a study seeking to isolate electrostatic phenomena. Prior failures to neutralize all the HCl after thiol-ene reactions involving DMAET-HCl resulted in final zwitterionic materials with reduced thermal stability and inconsistent phase behavior. Complete neutralization of HCl is evidenced by an incredibly sharp DMA peak in <sup>1</sup>H NMR (peak q in Figure S1), at least in non-polar solvents like CDCl<sub>3</sub>. DMAET-HCl samples were originally purified by dialysis before neutralizing the HCl with a hydroxide exchange resin, but this often resulted in low yields due to dialysis bags rupturing or leaking because of excessive osmotic pressures. The purification technique was then refined to a liquid-liquid extraction process which neutralized the HCl and removed ionic impurities concurrently, in addition to drastically improving yields. After thorough purification, neutralization of HCl, and drying, <sup>1</sup>H NMR analysis was used to calculate the reported zwitterion compositions based on butyl:DMA ratios. In terms of reactivity between thiol reagents, the calculated ratios were nearly identical to feed ratios into the thiol-ene reaction. The final sulfobetaine (SB) zwitterionic moiety was then obtained by the aprotic ring-opening reaction between 1,3-propanesultone and the nucleophilic dimethylamine group. On An additional discussion on synthetic troubleshooting can be found in the supporting information.

Using these methods, three resulting charge-neutral BPs were derived from the same PEO-*b*-PAGE backbone and are thus all expected to have similar dispersities ( $D = M_w/M_n \approx 1.27$ ) and comprise the same number average degree of polymerization ( $N_{EO} = 113$ ,  $N_{AGE} = 47.1$ ). Molecular weights and compositions were calculated using <sup>1</sup>H NMR spectroscopy while dispersity of the parent PEO-PAGE diblock copolymer was calculated using the differential refractive index detector from SEC which was universally calibrated with polystyrene standards. Samples are denoted as SB5, SB10, and SB17, containing charge fractions

([SB]/[AGE] x 100%) spanning 5-17 mol%, an overall  $M_n$  = 14.8-15.6 kDa, and PEO block compositions,  $wt_{PEO}$  = 0.31-0.33.

## **Phase Behavior vs Zwitterion Content**

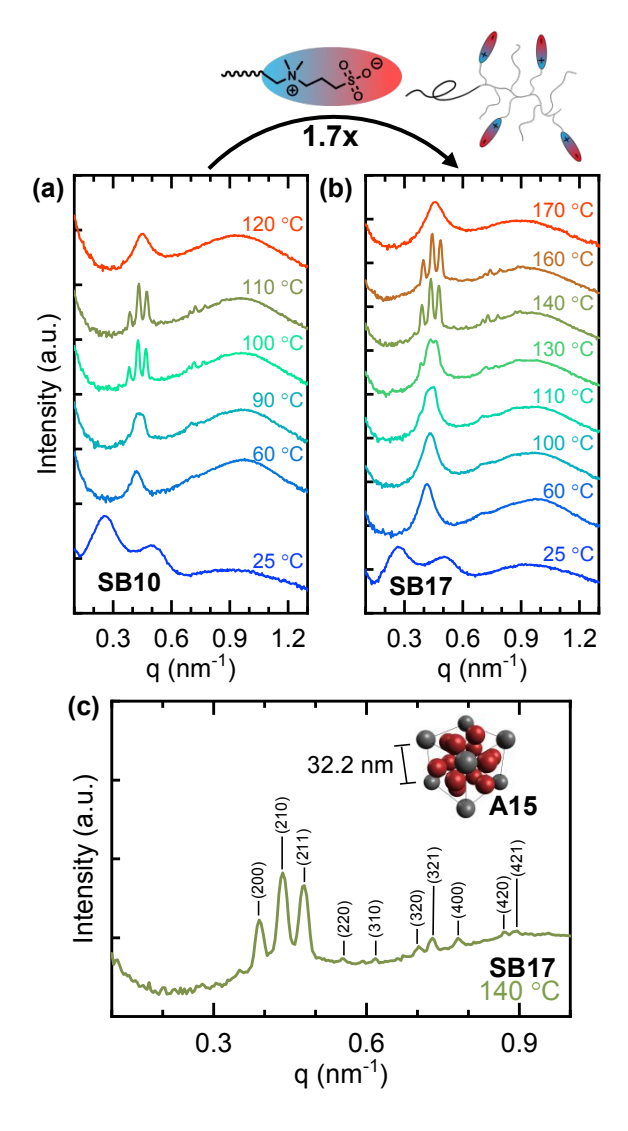


**Figure 1.** SAXS profiles taken at discrete temperatures (10 min anneal, 20 min exposure) upon heating from the semi-crystalline state for (a) SB10, (b) SB17, and (c) SB17 at 140 °C with the most apparent A15 peaks demarcated by Miller indices resulting from a lattice parameter, a = 32.2 nm.

The phase behavior of zwitterionic BPs was examined using SAXS at discrete temperature intervals starting from 25 °C and ending just above the order-disorder transition temperature (T<sub>ODT</sub>) (Figure 1). At 25 °C, PEO is semi-crystalline and both SB10 and SB17 exhibit two broad peaks (bottom traces in Figures

1a,b) with scattering vector magnitudes having ratios of 2:1, indicating the presence of weakly ordered lamellar morphologies. It is important to note that complete solvent evaporation and annealing were performed prior to any samples becoming semi-crystalline. Images of these room temperature morphologies were captured using AFM (Figure S4-S6). SB5 qualitatively displays the lamellar formations expected from "break-out crystallization" in BPs, where crystallization of one block is not confined by any thermally arrested state from a covalently neighboring phase. 108,109 SB10 contains—in addition to lamellar and particle phases—highly tortuous features akin to a heterogeneous disordered melt which reveals some level of confinement was at work during the structural arrest process of crystallizing PEO. Given SB10 has never entered the disordered regime up to this point in processing, this tortuous morphology also closely resembles that of a bicontinuous microemulsion. However, no equilibrium morphology of this nature has been reported for a BP without homopolymer doping, 110,111 although quenching from the disordered state has been utilized to obtain analogous morphologies. 112-114 An enlarged 5x5 µm AFM phase image is provided in Figure S5, illustrating the richness of phases present in this semi-crystalline sample. The rate of cooling to room temperature for SB10 was varied in a semi-qualitative fashion upon complete solvent evaporation during the film preparation process. The AFM images shown in Figure S4 were taken after cooling the samples very slowly from 70 °C to room temperature by simply switching off the heat on the vacuum oven while remaining under vacuum. When SB10 was removed from the oven (70 °C) to cool under ambient conditions (23 °C), no lamellar or particle phases were observed (Figure S6) throughout the course of the AFM experiment, only tortuous, aperiodic features.

Upon heating above  $T_{m,PEO}$  to 60 °C, ill-defined scattering profiles emerge in all samples with a broad, low symmetry peak consistent with the liquid-like packing (LLP) arrangement often observed in FK forming BPs after rapid cooling from a heterogeneous disordered state.<sup>54,57–60</sup> LLP is a non-equilibrium state which defines a disordered arrangement of micelles that can remain kinetically trapped for long periods of time below what is referred to as the ergodicity temperature, where chain exchange between micelles starts to diminish.<sup>51,59,69</sup> The appearance of the LLP state in this work likely arises kinetically as

the system transitions out of the frustrated morphology previously induced by PEO crystallization (recall AFM images in Figure S4). Crystallization and quenching from the disordered state can be viewed as somewhat synonymous with respect to forcing the system into a state of frustrated packing, a precursor to LLP. The zwitterionic block has a T<sub>g</sub> far below the crystallization temperature of PEO. Additionally, no observable thermal transitions related to ionic clusters were observed in the differential scanning calorimetry experiments (Figure S3). With no other thermally arrested phases, the crystallization of PEO will tend to flatten the interfacial curvature as crystallizing chains stack perpendicular to the phase interface. This preferential alignment of chains also helps explain the notably larger domain spacings in our semi-crystalline samples (23-31 nm at 25 °C) compared to those in the melt (14.9-15.2 nm at 60 °C), something which has been observed in other instances of "break-out crystallization" in block copolymers. 109,116,117

LLP can nucleate the formation of complex spherical phases such as a dodecagonal quasicrystal (DDQC) or FK phase over classic morphologies (e.g. BCC) given there is enough thermal energy to promote chain transfer.<sup>56,59</sup> Incidentally, we see what closely resembles a DDQC pattern develop in SB10 at 90 °C (Figure 1a) and SB17 at 110 °C (Figure 1b); although, the signal-to-noise and peak resolution are insufficient for peak fitting, comparison of the SB17 pattern at 120 °C to calculated DDQC indices (Figure S12) demonstrates good alignment. These DDQC designations are also consistent with experimental and theoretical findings for quenched BPs, <sup>58,59,61,62,65,70,71,75</sup> and for more analogous BPs which were heated from a semi-crystalline state.<sup>118</sup>

Always preceded by LLP, the DDQC phase has been shown to be metastable, often evolving into the  $\sigma$  phase, although a DDQC to A15 transition has been observed in a few instances. Possible reasoning behind why the A15 phase is favored over the  $\sigma$  phase is provided in the last chapter of this section. Succeeding the DDQC phase, SB10 and SB17 both exhibit the A15 phase prior to disordering by approximately 20 and 30 °C, respectively (Figure 1a,b). The resulting transition pathway upon heating for both samples is thus, LAM $\rightarrow$ LLP $\rightarrow$ DDQC $\rightarrow$ A15 $\rightarrow$ DIS. As a brief overview of this phase behavior; the

frustrated LAM morphology induced by PEO crystallization is thought to assist in the formation of disordered micelles (LLP) upon melting, thereby placing the system into a kinetically driven transition pathway (LLP→DDQC→) until the equilibrium A15 phase is reached.

Observation of FK phases in ion-containing systems has so far been incredibly rare and quite sensitive to variations in charge content. 89,93 This is partly due to the often narrow compositional window of such phases, but also due to the significant influence electrostatics have on the self-assembly of multicomponent systems. 33,119 In this work, persistence of the A15 phase after increasing zwitterion fraction 1.7x from SB10 to SB17, indicates that increasing zwitterion content from 10 to 17 mol% did not significantly skew the location of ordered phases along the compositional axis. However, theoretical insights from Kumar and Fredrickson suggests conformation (i.e.  $R_g \propto b$ ) of the zwitterion-tethered block may have decreased with increasing zwitterion content 120 which should result in a broadening of the A15 phase along the compositional axis. 53 The increased transition temperature into the A15 phase along with the increased  $T_{\rm ODT}$  between SB10 and SB17, together demonstrate vertical (i.e.,  $\chi$ N) shifting of phase boundaries with respect to zwitterion content while also indicating there is an upper  $\chi$ N boundary to the A15 phase. Vertical  $\chi$ N shifting from electrostatics can be explained using theoretical underpinnings while the upper  $\chi$ N boundary (low temperature) for the A15 phase is expected to be related to chain transfer kinetics. 51.59,69

Understanding why zwitterions produce vertical  $\chi N$  shifts in the phase boundary is crucial to understanding how they can be utilized to manipulate the phase behavior of ion-containing BPs. Since FK phase have so far proven to be highly sensitive to variations in charge content, we present evidence that zwitterions do not necessarily follow the same trend as other ionic species. Theoretical models have revealed that phase asymmetry in ion-containing block polymers relies heavily on entropic effects. For charge-pendant BPs, Sing et al. denoted counterion entropy to be the dominating factor which destabilized ordering at higher charged block compositions while electrostatic cohesion (enthalpic) stabilizes ordering at low charged block compositions. <sup>19,121</sup> For salt-doped BPs with a large ion-solvation preference into one

of the phases. Hou at al. observed ordering to be less stable at greater compositions of the ion solvating block due to the competition between solvation free energy and ion translational entropy.<sup>22</sup> Zwitterions present a unique class of ions with minimal 'counter'-ion translational entropy, owing to the covalent bond connecting the cation and anion. Tethering zwitterions to the polymer backbone further reduces ion-pair translational entropy and would thus be expected to produce more vertical reductions in  $(\gamma N)_{ODT}$  (i.e. increased T<sub>ODT</sub>) as zwitterion content increases. This type of behavior has been demonstrated experimentally by Ding et al. in high χ, low N zwitterion-tethered BPs. 122 However, our resulting phase behavior deviates substantially from that observed by Ding et al., likely due to differences in architecture. Their system contains zwitterions which are closely bound to the polymer backbone. The polyzwitterionic block in this study tethers zwitterions to the backbone via long, flexible linkages which should decrease its statistical segment length in addition to increasing the translational degrees of freedom of the zwitterionic moiety relative to one which is tethered closer to the backbone. The long interconnecting linkage promotes conformational asymmetry while the increased translational degrees of freedom limits segregation strength via entropic penalties. Thus, it is expected that the complex spherical packing observed in this study is owed more to architectural asymmetry while electrostatic interactions between zwitterions predominantly govern segregation strength (i.e.,  $\chi \propto 1/T_{\rm ODT}$ ).

The molecular weight of polymers in this study are greater than most FK-forming BPs reported. Unless conformational asymmetry is considerably increased for linear dBPs with narrow dispersity, the formation of FK phases is limited to an invariant degree of polymerization of N<100 ( $\approx$  10 kDa) and is directly related to entanglement melt dynamics. Micelles within FK phases must conform to several low-symmetry shapes for the purpose of filling space uniformly, and consequently impart a significant amount of packing frustration to the polymer chains. A relatively broader molecular weight distribution can help stabilize these complex geometries by providing additional degrees of freedom required to form various particle sizes and shapes. Hence, a modest increase in dispersity in our samples relative to most other studies (D = 1.27 vs < 1.1) is likely aiding in the stabilization of FK phases at higher molecular

weights compared to others of similar architecture.<sup>53,75,83,124</sup> One additional aspect to consider is the shape and symmetry of the dispersity profile (Figure S2). A slight protrusion at approximately twice the molecular weight of the primary peak indicates low levels of triblock copolymer which could tip the balance towards one FK phase over another within this realm of the phase space. Barbon et al. observed an unexpected broadening of the A15 phase vs. composition for their triblocks (interstitial block having lower *b*) relative to their diblocks, and noted fluctuation effects as a likely culprit.<sup>83</sup> Their data implies a favoritism towards the A15 phase in our samples due to the presence of triblock copolymer.

# **Dielectric Properties and Phase Transitions**

Dielectric relaxation spectroscopy measurements were performed by cycling the applied potential (0.1 V) between  $10^{-2}$ - $10^6$  Hz at discrete temperatures in the direction of cooling from  $110 \,^{\circ}$ C to  $30 \,^{\circ}$ C. Phase

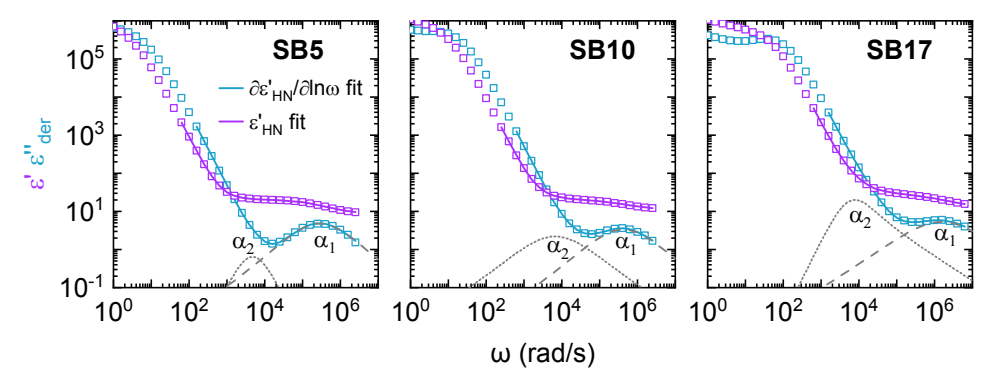


**Figure 2.** Real permittivity  $(\epsilon')$  and derivative loss  $(\epsilon')_{der}$  data at 50 °C for all denoted samples. Solid colored lines represent full fits (blue,  $\epsilon')_{der}$ ) and partial fits (purple,  $\epsilon'$ ) to the respective forms of the Havriliak-Negami (HN) function while dotted gray lines represent the respective peak terms within the HN function. For clarity, power law  $(A\omega^{-n})$  terms are not shown. Fitting and calculation details are provided in the supporting information along with fits at all temperatures.

equilibrium at each temperature was inferred by observation of overlapping  $\tan(\delta) = \epsilon''/\epsilon'$  traces between three successive frequency scans separated by 10 min intervals. The relaxation processes associated with ions and polymer chains are well described by their respective dielectric loss peaks. <sup>125</sup> In order to properly resolve the observable segmental ( $\alpha$ ) relaxation processes, the derivative formalism ( $\epsilon''_{der} = -\binom{\pi}{2}\partial\epsilon'/\partial ln\omega$ ) was utilized which removes much of the Ohmic/conductivity contributions from the dielectric loss spectra. <sup>126</sup> The resulting  $\epsilon''_{der}$  curves were fit to the proper form of the Havriliak-Negami (HN) function <sup>125</sup>- <sup>127</sup> in addition to a simple power law function to account for contributions from electrode polarization. Exact fitting equations, procedural discussion, and all fitting results can be found in the supporting information.

Figure 2 shows example fits at 50 °C to the respective HN functions for  $\varepsilon'$  and  $\varepsilon''_{der}$ , along with HN-peak functions obtained from the  $\partial \varepsilon'_{HN}/\partial ln\omega$  fit. Two relaxation processes were uncovered in all three samples, one preceding electrode polarization and the other partially convoluted by it. These two peaks are immediately apparent in  $\varepsilon''_{der}$  for SB10  $\geq$  100 °C (Figure S10b). The appearance of two relaxation processes is not uncommon for zwitterionic materials.<sup>84,128</sup> To confirm the validity of the implemented fitting procedures, all HN-peak parameters ( $\Delta \varepsilon$ ,  $\tau_{HN}$ , a, b) obtained from fitting to  $\varepsilon''_{der}$  were set as constants in the partial fitting to  $\varepsilon'$  across all temperatures (Figure S10). Thus, the only adjustable parameters for the

attainment of the  $\epsilon'_{HN}$  fits were the infinite dielectric constant ( $\epsilon_{\infty}$ ) and those from the power law term for electrode polarization. It should be noted that the " $\epsilon_{\infty}$ " fitting parameter contains all relaxation processes above the maximum frequency probed, including backbone relaxation from PEO and/or PAGE. Excellent overlap of the partially fitted  $\epsilon'_{HN}$  curve with the raw  $\epsilon'$  data in Figure 2 demonstrates that the HN parameters obtained are in reasonable agreement with reality.

The two relaxation processes observed substantially contribute to  $\varepsilon_s$  which implies they are both dominated by zwitterionic dipoles rather than backbone dipoles. It is evident from Figure 3b that there is a trade-off between the two relaxation processes with respect to temperature which only becomes evident at higher zwitterion contents (SB17), given this same trade-off is not apparent in SB5 (Figure 4a) and SB10 (Figure 4b). Such a significant temperature-dependent interchange between the two processes introduces the possibility that the  $\alpha_2$  relaxation represents zwitterionic aggregation in some way, while the faster  $\alpha_1$ 

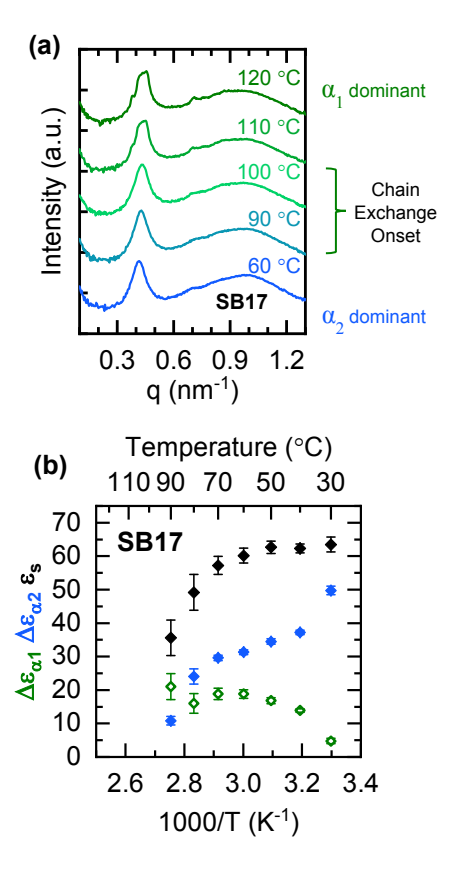


**Figure 3.** SB17 (a) SAXS profiles observed upon heating up to 120 °C and (b) dielectric strength ( $\Delta\epsilon$ ) for the  $\alpha_1$  (green) and  $\alpha_2$  (blue) relaxation processes, alongside the overall static dielectric constant ( $\epsilon_s$ ) calculated from DRS measurements taken after cooling from 120 °C. The onset of chain exchange between micelles in SB17, evidenced by the LLP  $\rightarrow$  DDCC transition observed 90 SAXS, correlates to the temperature range at which  $\Delta\epsilon_{\alpha 2}$  deteriorates and becomes dominated by  $\Delta\epsilon_{\alpha 1}$  (dotted box).

process may then be related to zwitterions able to relax with less restraint from surrounding interactions or bonds.

Figure 3 compares the dielectric response to the phase behavior within the relevant temperature range for SB17. The dielectric strength of the  $\alpha_2$  process ( $\Delta\epsilon_{\alpha 2}$ ) for SB17 follows a unique quadratic trend with respect to inverse temperature which declines rapidly ~ 80 °C with increasing temperature (Figure 3b). A very similar trend was recently observed by Scott et al. in a random copolymer with 10 mol\% zwitterionic functionality along the backbone, where  $\varepsilon_s$  rapidly declined above 80 °C, aligning directly with the tan( $\delta$ ) = G"/G' peak observed from dynamic mechanical analysis. 129 Such a correlation suggests zwitterionic interactions substantially weaken in proportion to the decline in their dielectric strength. In relation to this work, zwitterionic interactions are expected to play a predominant role in phase transition kinetics, especially at higher charge contents (i.e., SB17). Hence, the deterioration of physical zwitterionic crosslinks should allow phase transitions to commence. Transitioning out of the LLP state requires chain exchange between micelles to equilibrate into the complex particle shapes and sizes which exist within FK phases. Thus, this phase transition is kinetically limited and begins at some temperature which has been referred to as the ergodicity temperature. For SB17, this occurs < 110 °C, the temperature at which the DDQC phase becomes noticeable in Figure 3a. Between 80-90 °C, there is a crossover between  $\Delta \varepsilon_{\alpha 1}$  and  $\Delta \varepsilon_{a2}$  which coincides with a rapid decline in  $\Delta \varepsilon_{a2}$  with increasing temperature. These transitions in dielectric response appear to correlate to the onset of chain exchange required to transition out of the kinetically trapped LLP state (Figure 3).

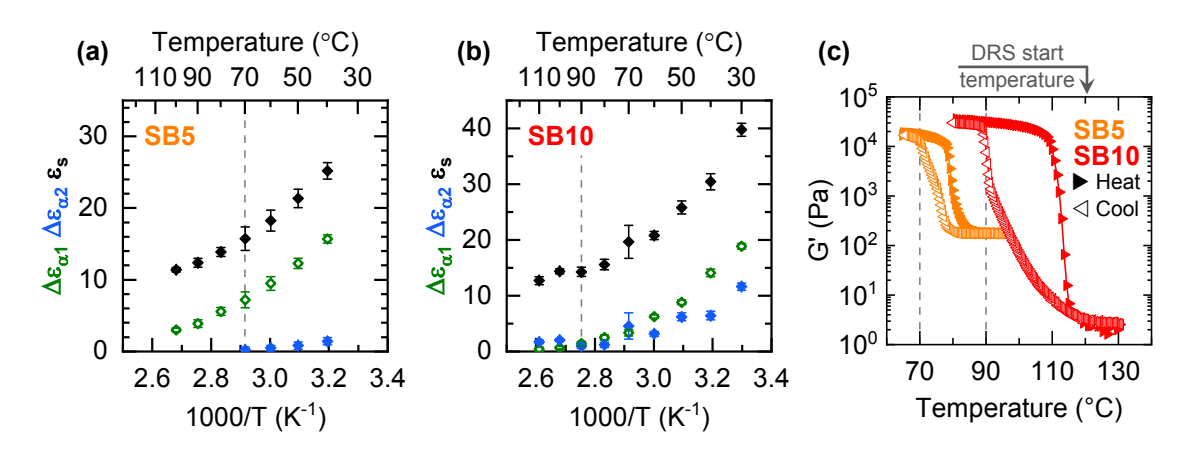
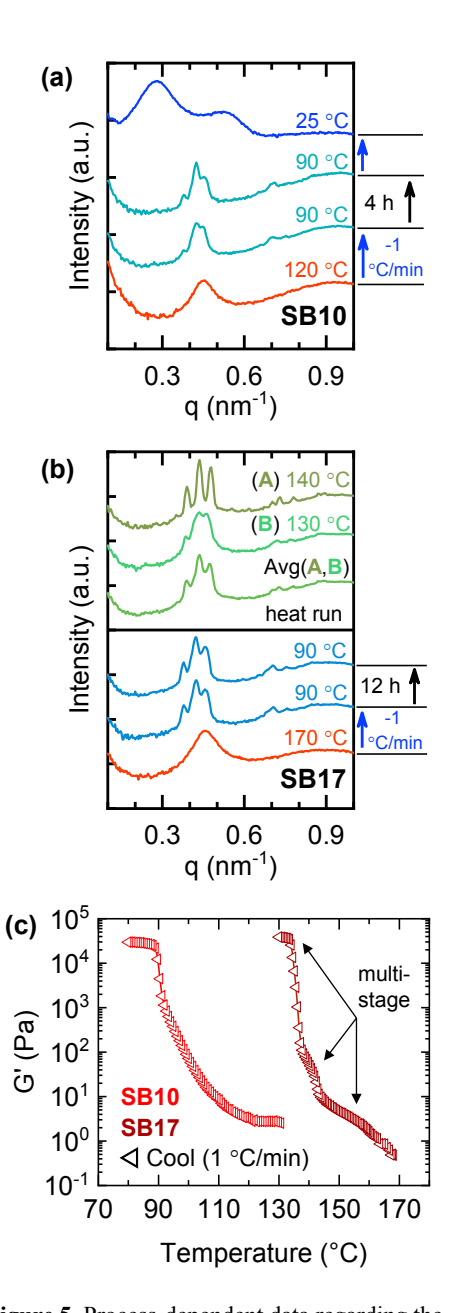


Figure 4. Temperature-dependent dielectric strength of the  $\alpha_1$  ( $\Delta\epsilon_{\alpha 1}$ ) and  $\alpha_2$  ( $\Delta\epsilon_{\alpha 2}$ ) relaxation processes, along with the total static dielectric constant ( $\epsilon_s$ ) are shown for (a) SB5 and (b) SB10, and compared to (c) the respective isochronal (1 rad/s), temperature-dependent storage modulus (G') at low shear (1%). Discrete DRS equilibrium measurements were taken upon cooling from an original temperature of 120 °C and denoted in (c) for proper comparison.

The decrease in zwitterion content from SB17 to SB10 coincides with a drastic transformation in dielectric behavior from highly coupled relaxation processes to more ideal trends in  $\varepsilon_s$ . However, there still exist indicators which express zwitterionic involvement in microphase transitioning. For SB5, the  $\alpha_2$  peak is only observed  $\leq 70$  °C with its dielectric strength ( $\Delta \varepsilon_{\alpha 2}$ ) increasing with decreasing temperature (Figure 4a). For SB10, there is a crossover between  $\Delta \varepsilon_{\alpha 1}$  and  $\Delta \varepsilon_{\alpha 2}$  at 90 °C (Figure 4b). Both phenomena align directly with the rheologically measured disorder-to-order transitions observed upon cooling for the respective samples (Figure 4c) which further establishes a relationship between the two phenomena. Details of this relationship are currently being explored and will form the basis of future work.

## **Phase Reversibility**



**Figure 5.** Process-dependent data regarding the reversibility of FK phases upon cooling from the disordered melt for SB10 and SB17. (a) SAXS profiles and processing conditions for SB10 showing a partial reemergence of the A15 phase after isothermally annealing at 90 °C for 4 h. (b) SAXS profiles and processing conditions for SB17 are qualitatively compared to a weight averaged profile calculated from its 130 °C (DDQC) and 140 °C (A15) SAXS profiles taken upon heating (Figure 1b). (c) Rheological isochronal temperature ramps for SB10 and SB17 showing the respective disorder-to-order transition behavior in G'.

To determine the equilibrium nature of the A15 phase in these systems, SAXS samples were slowly cooled from the disordered state at 1 °C/min to 90 °C for SB10 and SB17 and isothermally annealed there for an extended period as depicted in Figure 5. Partial reemergence of the A15 phase was observed in both samples which suggests the A15 phase is an equilibrium morphology for this system. In Figure 5c, the threshold of the G' plateau for SB10 at 90 °C indicates it has just entered the ordered regime at the start of 90 °C SAXS measurements in Figure 5a. Its SAXS profiles appear consistent with a DDQC phase which partially transitions into an A15 phase after 4 h. The rheological cooling ramp for SB17 (Figure 5c) indicates that 90 °C is well within the ordered regime for this sample while its SAXS profile at equivalent processing conditions demonstrates an ill-defined A15 phase. Qualitative comparison to a weighted average of the DDQC (130 °C) and A15 (140 °C) SAXS profiles for SB17 taken upon heating (Figure 1b) suggests this reemergent phase to be a coexistence of A15 and DDQC phases.

The multi-stage disorder-to-order transition observed rheologically (Figure 5c) may reflect the occurrence of a similar microphase transition pathway as that observed upon heating from the semi-crystalline state (i.e. LLP $\rightarrow$ DDQC $\rightarrow$ A15) which would align with findings by Mueller et al. <sup>118</sup> However, Mueller at al. obtained the  $\sigma$  phase upon cooling by rapidly quenching from the disordered state whereas we slowly cooled from the disordered state at 1 °C/min to obtain a partial reemergence of the A15 phase. In contrast, the A15 phase could have nucleated directly from the disordered state, comparable to observations by Bates et al. <sup>53</sup> In this scenario, the supposed DDQC phase would encompass a separate nucleation event; a reasonable outcome given the DDQC phase more closely resembles the  $\sigma$  phase than it does the A15 phase. Since SB17 does not conform to a well-defined structure over the course of 12 h provides another indication that zwitterions impose kinetically arresting interactions. Considering analyses from Figure 3 which illustrates kinetic effects to be less prominent  $\geq$  110 °C alongside declines in  $\varepsilon$ <sub>s</sub>, one might expect the ill-defined A15 phase for SB17 at 90 °C (Figure 5b) to either become more well-defined or continue transitioning into another ordered morphology by increasing temperature from 90 °C to  $\geq$  110 °C.

#### **CONCLUSIONS**

The relatively simple synthetic platform developed in this work permits the tunability of block chemistry, conformation, charge content, and polarity without significantly affecting backbone characteristics. Given the vast library of thiol-functional reagents, this platform can be easily extended to study targeted effects using an extensive array of chemical and architectural modifications. This platform was used to gain thermodynamic understanding of zwitterionic interactions and their influence on block polymer phase behavior and dielectric properties. Heating from the semi-crystalline state resulted in a LAM $\rightarrow$ LLP $\rightarrow$ DDQC $\rightarrow$ A15 $\rightarrow$ DIS transition pathway for samples with 10 and 17 mol% zwitterion content with valuable temperature-dependent correlations drawn between  $\epsilon_s$  and chain mobility. This 1.7-fold increase in zwitterion content did not destabilize the A15 phase which highlights the potential use of zwitterions in applications involving FK phases. Ill-defined A15 phases reemerged upon slowly cooling from the disordered state, suggesting it to be an equilibrium morphology for this system. The findings generated herein are fundamental to the design and regulation of phase behavior in block polymers while also stimulating the value of zwitterionic BPs in electroactive soft material applications.

#### ASSOCIATED CONTENT

# **Supporting Information**

Synthetic troubleshooting and molecular, thermal, morphological, and electrochemical characterization data including <sup>1</sup>H NMR, gel permeation chromatography, differential scanning calorimetry, atomic force microscopy, small-angle x-ray scattering, rheology, and dielectric relaxation spectroscopy. Python script for calculating DDQC peak positions is provided.

#### **AUTHOR INFORMATION**

# **Corresponding Author**

**Matthew D. Green** - Chemical Engineering, School for Engineering of Matter, Transport and Energy, Arizona State University, Tempe, AZ 85287, USA; Email: mdgreen8@asu.edu

#### **Authors**

**Bradley Grim** - Chemical Engineering, School for Engineering of Matter, Transport and Energy, Arizona State University, Tempe, AZ 85287, USA

Frederick L. Beyer - U.S. Army Research Laboratory, Aberdeen Proving Ground, MD 21005, USA

## **ACKNOWLEDGMENTS**

Special thanks to Greg Tudryn for all his help in making this work come to life. His lessons in dielectric relaxation spectroscopy methodology and analysis, in addition to his many helpful comments during the draft stage were invaluable. The authors would like to thank the National Science Foundation for supporting this work through Grant No. 1848454.

## REFERENCES

- (1) Helfand, E.; Tagami, Y. Theory of the Interface between Immiscible Polymers. II. *J. Chem. Phys.* **1972**, *56* (7), 3592–3601. https://doi.org/10.1063/1.1677735.
- (2) Leibler, L. Theory of Microphase Separation in Block Copolymers. *Macromolecules* **1980**, *13* (6), 1602–1617. https://doi.org/10.1021/ma60078a047.

- (3) Matsen, M. W.; Schick, M. Stable and Unstable Phases of a Diblock Copolymer Melt. *Phys. Rev. Lett.* **1994**, 72 (16), 2660–2663. https://doi.org/10.1103/PhysRevLett.72.2660.
- (4) Matsen, M. W.; Bates, F. S. Unifying Weak- and Strong-Segregation Block Copolymer Theories. *Macromolecules* **1996**, *29* (4), 1091–1098. https://doi.org/10.1021/ma951138i.
- (5) Matsen, M. W.; Bates, F. S. Block Copolymer Microstructures in the Intermediate-Segregation Regime. *J. Chem. Phys.* **1997**, *106* (6), 2436–2448. https://doi.org/10.1063/1.473153.
- (6) Maurer, W. W.; Bates, F. S.; Lodge, T. P.; Almdal, K.; Mortensen, K.; Fredrickson, G. H. Can a Single Function for χ Account for Block Copolymer and Homopolymer Blend Phase Behavior? J. Chem. Phys. 1998, 108 (7), 2989–3000. https://doi.org/10.1063/1.475704.
- (7) Cochran, E. W.; Garcia-Cervera, C. J.; Fredrickson, G. H. Stability of the Gyroid Phase in Diblock Copolymers at Strong Segregation. *Macromolecules* 2006, 39 (7), 2449–2451. https://doi.org/10.1021/ma0527707.
- (8) Semenov, A. N. Contribution to the Theory of Microphase Layering in Block-Copolymer Melts. *Zh. Eksp. Teor. Fiz* **1985**, *88*, 1242–1256.
- (9) Fredrickson, G. H.; Helfand, E. Fluctuation Effects in the Theory of Microphase Separation in Block Copolymers. *J. Chem. Phys.* **1987**, *87* (1), 697–705. https://doi.org/10.1063/1.453566.
- (10) Fredrickson, G. H.; Leibler, L. Theory of Block Copolymer Solutions: Nonselective Good Solvents. *Macromolecules* 1989, 22 (3), 1238–1250. https://doi.org/10.1021/ma00193a040.
- (11) Semenov, A. N. Microphase Separation in Diblock-Copolymer Melts: Ordering of Micelles. *Macromolecules* **1989**, *22* (6), 2849–2851. https://doi.org/10.1038/238056a0.
- Bates, F. S.; Fredrickson, G. H. Block Copolymer Thermodynamics: Theory and Experiment.
   Annu. Rev. Phys. Chem. 1990, 41 (1), 525–557.
   https://doi.org/10.1146/annurev.pc.41.100190.002521.

- (13) Mayes, A. M.; de la Cruz, M. O. Concentration Fluctuation Effects on Disorder–Order Transitions in Block Copolymer Melts. *J. Chem. Phys.* 1991, 95 (6), 4670–4677. https://doi.org/10.1063/1.461736.
- (14) Tang, H.; Freed, K. F. Interfacial Studies of Incompressible Binary Blends. *J. Chem. Phys.* **1991**, 94 (9), 6307–6322. https://doi.org/10.1063/1.460419.
- (15) Vavasour, J. D.; Whitmore, M. D. Self-Consistent Field Theory of Block Copolymers with Conformational Asymmetry. *Macromolecules* 1993, 26 (25), 7070–7075. https://doi.org/10.1021/ma00077a054.
- (16) Bates, F. S.; Fredrickson, G. H. Block Copolymers-Designer Soft Materials. *Phys. Today* **1999**, *52* (2), 32–38. https://doi.org/10.1063/1.882522.
- (17) Russell, T. P.; Karis, T. E.; Gallot, Y.; Mayes, A. M. A Lower Critical Ordering Transition in a Diblock Copolymer Melt. *Nature* **1994**, *368* (6473), 729–731. https://doi.org/10.1038/368729a0.
- (18) Matsen, M. W. Phase Behavior of Block Copolymer/Homopolymer Blends. *Macromolecules* **1995**, *28* (17), 5765–5773. https://doi.org/10.1021/ma00121a011.
- (19) Sing, C. E.; Zwanikken, J. W.; Olvera De La Cruz, M. Electrostatic Control of Block Copolymer Morphology. *Nat. Mater.* **2014**, *13* (7), 694–698. https://doi.org/10.1038/nmat4001.
- (20) Tang, J.; Jiang, Y.; Zhang, X.; Yan, D.; Chen, J. Z. Y. Phase Diagram of Rod-Coil Diblock Copolymer Melts. *Macromolecules* **2015**, *48* (24), 9060–9070. https://doi.org/10.1021/acs.macromol.5b02235.
- (21) Jung, H. Y.; Mandal, P.; Jo, G.; Kim, O.; Kim, M.; Kwak, K.; Park, M. J. Modulating Ion Transport and Self-Assembly of Polymer Electrolytes via End-Group Chemistry. *Macromolecules* 2017, 50 (8), 3224–3233. https://doi.org/10.1021/acs.macromol.7b00249.
- (22) Hou, K. J.; Qin, J. Solvation and Entropic Regimes in Ion-Containing Block Copolymers.

- Macromolecules 2018, 51 (19), 7463–7475. https://doi.org/10.1021/acs.macromol.8b01616.
- (23) Hou, K. J.; Loo, W. S.; Balsara, N. P.; Qin, J. Comparing Experimental Phase Behavior of Ion-Doped Block Copolymers with Theoretical Predictions Based on Selective Ion Solvation. *Macromolecules* 2020, *53* (10), 3956–3966. https://doi.org/10.1021/acs.macromol.0c00559.
- (24) Lequieu, J.; Koeper, T.; Delaney, K. T.; Fredrickson, G. H. Extreme Deflection of Phase
   Boundaries and Chain Bridging in A(BA')n Miktoarm Star Polymers. *Macromolecules* 2020, 53
   (2), 513–522. https://doi.org/10.1021/acs.macromol.9b02254.
- (25) Matsen, M. W. Stabilizing New Morphologies by Blending Homopolymer with Block Copolymer. *Phys. Rev. Lett.* **1995**, *74* (21), 4225–4228. https://doi.org/10.1103/PhysRevLett.74.4225.
- Zheng, W.; Wang, Z. G. Morphology of ABC Triblock Copolymers. *Macromolecules* 1995, 28
   (21), 7215–7223. https://doi.org/10.1021/ma00125a026.
- (27) Ruzette, A. V. G.; Banerjee, P.; Mayes, A. M.; Russell, T. P. A Simple Model for Baroplastic Behavior in Block Copolymer Melts. *J. Chem. Phys.* 2001, 114 (18), 8205–8209. https://doi.org/10.1063/1.1361072.
- (28) Ryu, D. Y.; Jeong, U.; Kim, J. K.; Russell, T. P. Closed-Loop Phase Behaviour in Block Copolymers. *Nat. Mater.* **2002**, *1* (2), 114–117. https://doi.org/10.1038/nmat724.
- (29) Grason, G. M.; DiDonna, B. A.; Kamien, R. D. Geometric Theory of Diblock Copolymer Phases. *Phys. Rev. Lett.* **2003**, *91* (5), 058304. https://doi.org/10.1103/PhysRevLett.91.058304.
- (30) Lynd, N. A.; Meuler, A. J.; Hillmyer, M. A. Polydispersity and Block Copolymer Self-Assembly. *Prog. Polym. Sci.* **2008**, *33* (9), 875–893. https://doi.org/10.1016/j.progpolymsci.2008.07.003.
- (31) Park, M. J.; Balsara, N. P. Phase Behavior of Symmetric Sulfonated Block Copolymers. *Macromolecules* **2008**, *41* (10), 3678–3687. https://doi.org/10.1021/ma702733f.

- (32) Matsen, M. W. Effect of Architecture on the Phase Behavior of AB-Type Block Copolymer Melts. *Macromolecules* **2012**, *45* (4), 2161–2165. https://doi.org/10.1021/ma202782s.
- (33) Grim, B. J.; Green, M. D. Thermodynamics and Structure–Property Relationships of Charged Block Polymers. *Macromol. Chem. Phys.* 2022, 223 (14), 2200036. https://doi.org/10.1002/macp.202200036.
- (34) Ketkar, P. M.; Epps, T. H. Nanostructured Block Polymer Electrolytes: Tailoring Self-Assembly to Unlock the Potential in Lithium-Ion Batteries. *Acc. Chem. Res.* 2021, 54 (23), 4342–4353. https://doi.org/10.1021/acs.accounts.1c00468.
- (35) Elabd, Y. A.; Hickner, M. A. Block Copolymers for Fuel Cells. *Macromolecules* **2011**, *44* (1), 1–11. https://doi.org/10.1021/ma101247c.
- (36) Lodge, T. P. Block Copolymers: Long-Term Growth with Added Value. *Macromolecules* **2020**, 53 (1), 2–4. https://doi.org/10.1021/acs.macromol.9b02069.
- (37) Kim, J.; Jung, H. Y.; Park, M. J. End-Group Chemistry and Junction Chemistry in Polymer Science: Past, Present, and Future. *Macromolecules* 2020, 53 (3), 746–763. https://doi.org/10.1021/acs.macromol.9b02293.
- (38) Wang, R. Y.; Park, M. J. Self-Assembly of Block Copolymers with Tailored Functionality: From the Perspective of Intermolecular Interactions. *Annu. Rev. Mater. Res.* 2020, 50, 521–549. https://doi.org/10.1146/annurev-matsci-081519-020046.
- (39) Liu, T.; Liu, G. Block Copolymers for Supercapacitors, Dielectric Capacitors and Batteries. *J. Phys. Condens. Matter* **2019**, *31* (23), 233001. https://doi.org/10.1088/1361-648X/ab0d77.
- (40) Ito, T.; Ghimire, G. Electrochemical Applications of Microphase-Separated Block Copolymer

  Thin Films. *ChemElectroChem* **2018**, *5* (20), 2937–2953. https://doi.org/10.1002/celc.201800576.
- (41) Bates, C. M.; Bates, F. S. 50th Anniversary Perspective: Block Polymers-Pure Potential.

- Macromolecules 2017, 50 (1), 3–22. https://doi.org/10.1021/acs.macromol.6b02355.
- (42) Radhakrishna, M.; Sing, C. E. Charge Correlations for Precise, Coulombically Driven Self Assembly. *Macromol. Chem. Phys.* 2016, 217 (2), 126–136. https://doi.org/10.1002/macp.201500278.
- (43) Meek, K. M.; Elabd, Y. A. Polymerized Ionic Liquid Block Copolymers for Electrochemical Energy. *J. Mater. Chem. A* **2015**, *3* (48), 24187–24194. https://doi.org/10.1039/c5ta07170d.
- (44) Matsen, M. W.; Bates, F. S. *Origins of Complex Self-Assembly in Block Copolymers*; 1996; Vol. 29. https://doi.org/10.1021/ma960744q.
- (45) Milner, S. T. Chain Architecture and Asymmetry in Copolymer Microphases. *Macromolecules* **1994**, *27* (8), 2333–2335. https://doi.org/10.1021/ma00086a057.
- (46) Bates, F. S.; Fredrickson, G. H. Conformational Asymmetry and Polymer-Polymer Thermodynamics. *Macromolecules* **1994**, *27* (4), 1065–1067. https://doi.org/10.1021/ma00082a030.
- (47) Matsen, M. W.; Bates, F. S. Conformationally Asymmetric Block Copolymers. *J. Polym. Sci. Part B Polym. Phys.* **1997**, *35* (6), 945–952. https://doi.org/10.1002/(SICI)1099-0488(19970430)35:6<945::AID-POLB9>3.0.CO;2-G.
- Pochan, D. J.; Gido, S. P.; Pispas, S.; Mays, J. W.; Ryan, A. J.; Fairclough, J. P. A.; Hamley, I.
   W.; Terrill, N. J. Morphologies of Microphase-Separated A2B Simple Graft Copolymers.
   Macromolecules 1996, 29 (15), 5091–5098. https://doi.org/10.1021/ma951696x.
- (49) Beyer, F. L.; Gido, S. P.; Velis, G.; Hadjichristidis, N.; Tan, N. B. Morphological Behavior of A 5 B Miktoarm Star Block Copolymers. *Macromolecules* 1999, 32 (20), 6604–6607. https://doi.org/10.1021/ma9909713.
- (50) Xie, N.; Li, W.; Qiu, F.; Shi, A. C. σ Phase Formed in Conformationally Asymmetric AB-Type

- Block Copolymers. ACS Macro Lett. 2014, 3 (9), 909–910. https://doi.org/10.1021/mz500445v.
- (51) Schulze, M. W.; Lewis, R. M.; Lettow, J. H.; Hickey, R. J.; Gillard, T. M.; Hillmyer, M. A.; Bates, F. S. Conformational Asymmetry and Quasicrystal Approximants in Linear Diblock Copolymers. *Phys. Rev. Lett.* 2017, 118 (20). https://doi.org/10.1103/PhysRevLett.118.207801.
- (52) Collanton, R. P.; Dorfman, K. D. Interfacial Geometry in Particle-Forming Phases of Diblock Copolymers. *Phys. Rev. Mater.* 2022, 6 (1), 015602. https://doi.org/10.1103/PhysRevMaterials.6.015602.
- Bates, M. W.; Lequieu, J.; Barbon, S. M.; Lewis, R. M.; Delaney, K. T.; Anastasaki, A.; Hawker, C. J.; Fredrickson, G. H.; Bates, C. M. Stability of the A15 Phase in Diblock Copolymer Melts.
  Proc. Natl. Acad. Sci. U. S. A. 2019, 116 (27), 13194–13199.
  https://doi.org/10.1073/pnas.1900121116.
- (54) Lee, S.; Bluemle, M. J.; Bates, F. S. Discovery of a Frank-Kasper σ Phase in Sphere-Forming Block Copolymer Melts. *Science* (80-.). 2010, 330 (6002), 349–353. https://doi.org/10.1126/science.1195552.
- (55) Huang, M.; Yue, K.; Wang, J.; Hsu, C. H.; Wang, L.; Cheng, S. Z. D. Frank-Kasper and Related Quasicrystal Spherical Phases in Macromolecules. *Sci. China Chem.* **2018**, *61* (1), 33–45. https://doi.org/10.1007/s11426-017-9140-8.
- (56) Dorfman, K. D. Frank-Kasper Phases in Block Polymers. *Macromolecules* **2021**, *54* (22), 10251–10270. https://doi.org/10.1021/acs.macromol.1c01650.
- (57) Lee, S.; Leighton, C.; Bates, F. S. Sphericity and Symmetry Breaking in the Formation of Frank-Kasper Phases from One Component Materials. *Proc. Natl. Acad. Sci. U. S. A.* **2014**, *111* (50), 17723–17731. https://doi.org/10.1073/pnas.1408678111.
- (58) Chanpuriya, S.; Kim, K.; Zhang, J.; Lee, S.; Arora, A.; Dorfman, K. D.; Delaney, K. T.;

- Fredrickson, G. H.; Bates, F. S. Cornucopia of Nanoscale Ordered Phases in Sphere-Forming Tetrablock Terpolymers. *ACS Nano* **2016**, *10* (5), 4961–4972. https://doi.org/10.1021/acsnano.6b00495.
- (59) Gillard, T. M.; Lee, S.; Bates, F. S. Dodecagonal Quasicrystalline Order in a Diblock Copolymer Melt. Proc. Natl. Acad. Sci. U. S. A. 2016, 113 (19), 5167–5172. https://doi.org/10.1073/pnas.1601692113.
- (60) Kim, K.; Schulze, M. W.; Arora, A.; Lewis, R. M.; Hillmyer, M. A.; Dorfman, K. D.; Bates, F. S. Thermal Processing of Diblock Copolymer Melts Mimics Metallurgy. *Science* (80-.). 2017, 356 (6337), 520–523. https://doi.org/10.1126/science.aam7212.
- (61) Lindsay, A. P.; Jayaraman, A.; Peterson, A. J.; Mueller, A. J.; Weigand, S.; Almdal, K.; Mahanthappa, M. K.; Lodge, T. P.; Bates, F. S. Reevaluation of Poly(Ethylene- Alt-Propylene)-Block-Polydimethylsiloxane Phase Behavior Uncovers Topological Close-Packing and Epitaxial Quasicrystal Growth. ACS Nano 2021, 15 (6), 9453–9468.
  https://doi.org/10.1021/acsnano.1c02420.
- (62) Zhang, C.; Vigil, D. L.; Sun, D.; Bates, M. W.; Loman, T.; Murphy, E. A.; Barbon, S. M.; Song, J. A.; Yu, B.; Fredrickson, G. H.; et al. Emergence of Hexagonally Close-Packed Spheres in Linear Block Copolymer Melts. *J. Am. Chem. Soc.* 2021, 143 (35), 14106–14114. https://doi.org/10.1021/jacs.1c03647.
- (63) Mueller, A. J.; Lindsay, A. P.; Jayaraman, A.; Lodge, T. P.; Mahanthappa, M. K.; Bates, F. S. Emergence of a C15 Laves Phase in Diblock Polymer/Homopolymer Blends. *ACS Macro Lett.* 2020, 9 (4), 576–582. https://doi.org/10.1021/acsmacrolett.0c00124.
- (64) Takagi, H.; Hashimoto, R.; Igarashi, N.; Kishimoto, S.; Yamamoto, K. Frank-Kasper σ Phase in Polybutadiene-Poly(ε-Caprolactone) Diblock Copolymer/Polybutadiene Blends. *J. Phys. Condens. Matter* 2017, 29 (20), 204002. https://doi.org/10.1088/1361-648X/aa6908.

- (65) Takagi, H.; Yamamoto, K. Phase Boundary of Frank-Kasper σ Phase in Phase Diagrams of Binary Mixtures of Block Copolymers and Homopolymers. *Macromolecules* 2019, 52 (5), 2007–2014. https://doi.org/10.1021/acs.macromol.8b02356.
- (66) Xie, J.; Shi, A. C. Formation of Complex Spherical Packing Phases in Diblock Copolymer/Homopolymer Blends. *Giant* 2021, 5, 100043. https://doi.org/10.1016/j.giant.2020.100043.
- (67) Cheong, G. K.; Bates, F. S.; Dorfman, K. D. Symmetry Breaking in Particle-Forming Diblock Polymer/Homopolymer Blends. *Proc. Natl. Acad. Sci. U. S. A.* 2020, 117 (29), 16764–16769. https://doi.org/10.1073/pnas.2006079117.
- (68) Liu, M.; Qiang, Y.; Li, W.; Qiu, F.; Shi, A. C. Stabilizing the Frank-Kasper Phases via Binary Blends of AB Diblock Copolymers. ACS Macro Lett. 2016, 5 (10), 1167–1171. https://doi.org/10.1021/acsmacrolett.6b00685.
- (69) Kim, K.; Arora, A.; Lewis, R. M.; Liu, M.; Li, W.; Shi, A. C.; Dorfman, K. D.; Bates, F. S. Origins of Low-Symmetry Phases in Asymmetric Diblock Copolymer Melts. *Proc. Natl. Acad. Sci. U. S. A.* 2018, 115 (5), 847–854. https://doi.org/10.1073/pnas.1717850115.
- (70) Lindsay, A. P.; Lewis, R. M.; Lee, B.; Peterson, A. J.; Lodge, T. P.; Bates, F. S. A15, σ, and a Quasicrystal: Access to Complex Particle Packings via Bidisperse Diblock Copolymer Blends.
  ACS Macro Lett. 2020, 9 (2), 197–203. https://doi.org/10.1021/acsmacrolett.9b01026.
- (71) Li, W.; Duan, C.; Shi, A. C. Nonclassical Spherical Packing Phases Self-Assembled from AB-Type Block Copolymers. ACS Macro Lett. 2017, 6 (11), 1257–1262. https://doi.org/10.1021/acsmacrolett.7b00756.
- (72) Ma, Z.; Tan, R.; Gan, Z.; Zhou, D.; Yang, Y.; Zhang, W.; Dong, X. H. Modulation of the Complex Spherical Packings through Rationally Doping a Discrete Homopolymer into a Discrete Block

- Copolymer: A Quantitative Study. *Macromolecules* **2022**, *55* (11), 4331–4340. https://doi.org/10.1021/acs.macromol.2c00682.
- (73) Qiang, Y.; Li, W.; Shi, A. C. Stabilizing Phases of Block Copolymers with Gigantic Spheres via Designed Chain Architectures. ACS Macro Lett. 2020, 9 (5), 668–673. https://doi.org/10.1021/acsmacrolett.0c00193.
- (74) Vigil, D. L.; Quah, T.; Sun, D.; Delaney, K. T.; Fredrickson, G. H. Self-Consistent Field Theory Predicts Universal Phase Behavior for Linear, Comb, and Bottlebrush Diblock Copolymers. *Macromolecules* 2022, 55 (11), 4237–4244. https://doi.org/10.1021/acs.macromol.2c00192.
- (75) Chang, A. B.; Bates, F. S. Impact of Architectural Asymmetry on Frank-Kasper Phase Formation in Block Polymer Melts. ACS Nano 2020, 14 (9), 11463–11472.
  https://doi.org/10.1021/acsnano.0c03846.
- (76) Watanabe, M.; Asai, Y.; Suzuki, J.; Takano, A.; Matsushita, Y. Frank-Kasper A15 Phase Formed in ABN Block-Graft Copolymers with Large Numbers of Graft Chains. *Macromolecules* 2020, 53 (22), 10217–10224. https://doi.org/10.1021/acs.macromol.0c01097.
- (77) Sun, Y.; Tan, R.; Ma, Z.; Gan, Z.; Li, G.; Zhou, D.; Shao, Y.; Zhang, W. Bin; Zhang, R.; Dong, X.
   H. Discrete Block Copolymers with Diverse Architectures: Resolving Complex Spherical Phases with One Monomer Resolution. *ACS Cent. Sci.* 2020, 6 (8), 1386–1393.
   https://doi.org/10.1021/acscentsci.0c00798.
- (78) Zhou, D.; Xu, M.; Ma, Z.; Gan, Z.; Zheng, J.; Tan, R.; Dong, X. H. Discrete Diblock Copolymers with Tailored Conformational Asymmetry: A Precise Model Platform to Explore Complex Spherical Phases. *Macromolecules* 2022, 55 (16), 7013–7022. https://doi.org/10.1021/acs.macromol.2c01202.
- (79) Bates, M. W.; Barbon, S. M.; Levi, A. E.; Lewis, R. M.; Beech, H. K.; Vonk, K. M.; Zhang, C.;

- Fredrickson, G. H.; Hawker, C. J.; Bates, C. M. Synthesis and Self-Assembly of ABn Miktoarm Star Polymers. *ACS Macro Lett.* **2020**, *9* (3), 396–403. https://doi.org/10.1021/acsmacrolett.0c00061.
- (80) Li, C.; Dong, Q.; Li, W. Largely Tunable Asymmetry of Phase Diagrams of A(AB) n Miktoarm Star Copolymer. *Macromolecules* 2020, 53 (24), 10907–10917. https://doi.org/10.1021/acs.macromol.0c02272.
- (81) Grason, G. M.; Kamien, R. D. Interfaces in Diblocks: A Study of Miktoarm Star Copolymers. *Macromolecules* **2004**, *37* (19), 7371–7380. https://doi.org/10.1021/ma049255d.
- (82) Lewis, R. M.; Arora, A.; Beech, H. K.; Lee, B.; Lindsay, A. P.; Lodge, T. P.; Dorfman, K. D.; Bates, F. S. Role of Chain Length in the Formation of Frank-Kasper Phases in Diblock Copolymers. *Phys. Rev. Lett.* 2018, *121* (20). https://doi.org/10.1103/PhysRevLett.121.208002.
- (83) Barbon, S. M.; Song, J. A.; Chen, D.; Zhang, C.; Lequieu, J.; Delaney, K. T.; Anastasaki, A.; Rolland, M.; Fredrickson, G. H.; Bates, M. W.; et al. Architecture Effects in Complex Spherical Assemblies of (AB)n-Type Block Copolymers. ACS Macro Lett. 2020, 9 (12), 1745–1752. https://doi.org/10.1021/acsmacrolett.0c00704.
- (84) Mei, W.; Rothenberger, A. J.; Bostwick, J. E.; Rinehart, J. M.; Hickey, R. J.; Colby, R. H. Zwitterions Raise the Dielectric Constant of Soft Materials. *Phys. Rev. Lett.* 2021, 127 (22), 228001. https://doi.org/10.1103/PhysRevLett.127.228001.
- (85) Jones, S. D.; Nguyen, H.; Richardson, P. M.; Chen, Y. Q.; Wyckoff, K. E.; Hawker, C. J.; Clément, R. J.; Fredrickson, G. H.; Segalman, R. A. Design of Polymeric Zwitterionic Solid Electrolytes with Superionic Lithium Transport. ACS Cent. Sci. 2022, 8 (2), 169–175. https://doi.org/10.1021/acscentsci.1c01260.
- (86) Kim, O.; Kim, K.; Choi, U. H.; Park, M. J. Tuning Anhydrous Proton Conduction in Single-Ion

- Polymers by Crystalline Ion Channels. *Nat. Commun.* **2018**, *9* (1), 5029. https://doi.org/10.1038/s41467-018-07503-4.
- (87) Kim, O.; Kim, H.; Choi, U. H.; Park, M. J. One-Volt-Driven Superfast Polymer Actuators Based on Single-Ion Conductors. *Nat. Commun.* 2016, 7. https://doi.org/10.1038/ncomms13576.
- (88) Jung, H. Y.; Kim, O.; Park, M. J. Ion Transport in Nanostructured Phosphonated Block Copolymers Containing Ionic Liquids. *Macromol. Rapid Commun.* 2016, 37 (14), 1116–1123. https://doi.org/10.1002/marc.201600036.
- (89) Min, J.; Jung, H. Y.; Jeong, S.; Lee, B.; Son, C. Y.; Park, M. J. Enhancing Ion Transport in Charged Block Copolymers by Stabilizing Low Symmetry Morphology: Electrostatic Control of Interfaces. *Proc. Natl. Acad. Sci.* 2021, 118 (32). https://doi.org/10.1073/pnas.2107987118.
- (90) Russell, S. T.; Raghunathan, R.; Jimenez, A. M.; Zhang, K.; Brucks, S. D.; Iacob, C.; West, A. C.; Gang, O.; Campos, L. M.; Kumar, S. K. Impact of Electrostatic Interactions on the Self-Assembly of Charge-Neutral Block Copolyelectrolytes. *Macromolecules* 2020, *53* (2), 548–557. https://doi.org/10.1021/acs.macromol.9b01293.
- (91) Wang, R. Y.; Zhang, Z. K.; Guo, X. S.; Cao, X. H.; Zhang, T. Y.; Tong, Z. Z.; Xu, J. T.; Du, B. Y.; Fan, Z. Q. Mechanistic Study of the Influence of Salt Species on the Lower Disorder-to-Order Transition Behavior of Poly(Ethylene Oxide)- b-Poly(Ionic Liquid)/Salt Hybrids. *Macromolecules* 2020, 53 (11), 4560–4567. https://doi.org/10.1021/acs.macromol.9b02576.
- (92) Cho, B. K.; Jain, A.; Gruner, S. M.; Wiesner, U. Mesophase Structure-Mechanical and Ionic Transport Correlations in Extended Amphiphilic Dendrons. *Science* (80-.). 2004, 305 (5690), 1598–1601. https://doi.org/10.1126/science.1100872.
- (93) Lodge, T. P.; Xie, S.; Lindsay, A. P.; Bates, F. S. Formation of a C15 Laves Phase with a Giant Unit Cell in Salt-Doped A/B/Ab Ternary Polymer Blends. *ACS Nano* **2020**, *14* (10), 13754–13764.

- https://doi.org/10.1021/acsnano.0c06071.
- (94) Jung, H. Y.; Park, M. J. Thermodynamics and Phase Behavior of Acid-Tethered Block Copolymers with Ionic Liquids. *Soft Matter* 2017, 13 (1), 250–257. https://doi.org/10.1039/C6SM00947F.
- (95) Min, J.; Barpuzary, D.; Ham, H.; Kang, G. C.; Park, M. J. Charged Block Copolymers: From Fundamentals to Electromechanical Applications. *Acc. Chem. Res.* 2021, 54 (21), 4024–4035. https://doi.org/10.1021/acs.accounts.1c00423.
- (96) Hillmyer, M. A.; Bates, F. S. Synthesis and Characterization of Model Polyalkane–Poly(Ethylene Oxide) Block Copolymers. *Macromolecules* 1996, 29 (22), 6994–7002. https://doi.org/10.1021/ma960774t.
- (97) Lee, B. F.; Kade, M. J.; Chute, J. A.; Gupta, N.; Campos, L. M.; Fredrickson, G. H.; Kramer, E. J.; Lynd, N. A.; Hawker, C. J. Poly(Allyl Glycidyl Ether)-A Versatile and Functional Polyether Platform. *J. Polym. Sci. Part A Polym. Chem.* 2011, 49 (20), 4498–4504. https://doi.org/10.1002/pola.24891.
- (98) Lee, B. F.; Wolffs, M.; Delaney, K. T.; Sprafke, J. K.; Leibfarth, F. A.; Hawker, C. J.; Lynd, N. A. Reactivity Ratios and Mechanistic Insight for Anionic Ring-Opening Copolymerization of Epoxides. *Macromolecules* 2012, 45 (9), 3722–3731. https://doi.org/10.1021/ma300634d.
- (99) Barteau, K. P.; Wolffs, M.; Lynd, N. A.; Fredrickson, G. H.; Kramer, E. J.; Hawker, C. J. Allyl Glycidyl Ether-Based Polymer Electrolytes for Room Temperature Lithium Batteries.
  Macromolecules 2013, 46 (22), 8988–8994. https://doi.org/10.1021/ma401267w.
- (100) Geng, Z.; Schauser, N. S.; Lee, J.; Schmeller, R. P.; Barbon, S. M.; Segalman, R. A.; Lynd, N. A.; Hawker, C. J. Role of Side-Chain Architecture in Poly(Ethylene Oxide)-Based Copolymers. *Macromolecules* 2020, 16, acs.macromol.0c01116.

- https://doi.org/10.1021/acs.macromol.0c01116.
- (101) Fetters, L. J. Procedures for Homogeneous Anionic Polymerization. *J. Res. Natl. Bur. Stand. Sect.*A Phys. Chem. **1966**, 70A (5), 421. https://doi.org/10.6028/jres.070a.035.
- (102) Hadjichristidis, N.; Iatrou, H.; Pispas, S.; Pitsikalis, M. Anionic Polymerization: High Vacuum Techniques. *J. Polym. Sci. Part A Polym. Chem.* 2000, 38 (18), 3211–3234.
  https://doi.org/10.1002/1099-0518(20000915)38:18<3211::AID-POLA10>3.0.CO;2-L.
- (103) Uhrig, D.; Mays, J. W. Experimental Techniques in High-Vacuum Anionic Polymerization. *J. Polym. Sci. Part A Polym. Chem.* **2005**, *43* (24), 6179–6222. https://doi.org/10.1002/pola.21016.
- (104) Yang, Y.; Ramos, T. L.; Heo, J.; Green, M. D. Zwitterionic Poly(Arylene Ether Sulfone)
  Copolymer/Poly(Arylene Ether Sulfone) Blends for Fouling-Resistant Desalination Membranes. J.
  Memb. Sci. 2018, 561, 69–78. https://doi.org/10.1016/j.memsci.2018.05.025.
- (105) Ilavsky, J. Nika: Software for Two-Dimensional Data Reduction. *J. Appl. Cryst* 2012, *45*, 324–328. https://doi.org/10.1107/S0021889812004037.
- (106) Ilavsky, J.; Jemian, P. R. Irena: Tool Suite for Modeling and Analysis of Small-Angle Scattering. *J. Appl. Crystallogr.* **2009**, *42* (2), 347–353. https://doi.org/10.1107/S0021889809002222.
- (107) Hoyle, C. E.; Bowman, C. N. Thiol-Ene Click Chemistry. *Angew. Chemie Int. Ed.* **2010**, 49 (9), 1540–1573. https://doi.org/10.1002/anie.200903924.
- (108) Loo, Y.; Register, R. A.; Ryan, A. J. Modes of Crystallization in Block Copolymer Microdomains: Breakout, Templated, and Confined. *Macromolecules* 2002, 35 (6), 2365–2374. https://doi.org/10.1021/ma011824j.
- (109) Xu, W.; Zheng, Y.; Pan, P. Crystallization-driven Self-assembly of Semicrystalline Block Copolymers and End-functionalized Polymers: A Minireview. *J. Polym. Sci.* 2022, 60 (15), 2136–2152. https://doi.org/10.1002/pol.20210789.

- (110) Bates, F. S.; Maurer, W. W.; Lipic, P. M.; Hillmyer, M. A.; Almdal, K.; Mortensen, K.; Fredrickson, G. H.; Lodge, T. P. Polymeric Bicontinuous Microemulsions. *Phys. Rev. Lett.* **1997**, 79 (5), 849–852. https://doi.org/10.1103/PhysRevLett.79.849.
- (111) Shim, J.; Bates, F. S.; Lodge, T. P. Bicontinuous Microemulsions in Partially Charged Ternary Polymer Blends. ACS Macro Lett. 2019, 8 (9), 1166–1171. https://doi.org/10.1021/acsmacrolett.9b00554.
- (112) Chan, W. Y.; Hillmyer, M. A. Disordered Triblock Polymers for Nanoporous Materials with Tunable Surface Properties for Ultrafiltration Applications. ACS Appl. Polym. Mater. 2022, 4 (11), 8009–8020. https://doi.org/10.1021/acsapm.2c00065.
- (113) Pitet, L. M.; Amendt, M. A.; Hillmyer, M. A. Nanoporous Linear Polyethylene from a Block Polymer Precursor. J. Am. Chem. Soc. 2010, 132 (24), 8230–8231. https://doi.org/10.1021/ja100985d.
- (114) Hillmyer, M. A. Nanoporous Materials from Block Copolymer Precursors. In *Block Copolymers II*; Springer-Verlag: Berlin/Heidelberg, 2005; Vol. 190, pp 137–181. https://doi.org/10.1007/12\_002.
- (115) DiMarzio, E. A.; Guttman, C. M.; Hoffman, J. D. Calculation of Lamellar Thickness in a Diblock Copolymer, One of Whose Components Is Crystalline. *Macromolecules* 1980, 13 (5), 1194–1198. https://doi.org/10.1021/ma60077a032.
- (116) Hong, S.; Yang, L.; MacKnight, W. J.; Gido, S. P. Morphology of a Crystalline/Amorphous Diblock Copolymer: Poly((Ethylene Oxide)-b-Butadiene). *Macromolecules* **2001**, *34* (20), 7009–7016. https://doi.org/10.1021/ma0100596.
- (117) Shiomi, T.; Takeshita, H.; Kawaguchi, H.; Nagai, M.; Takenaka, K.; Miya, M. Crystallization and Structure Formation of Block Copolymers Containing a Rubbery Amorphous Component.

- Macromolecules 2002, 35 (21), 8056–8065. https://doi.org/10.1021/ma0200118.
- (118) Mueller, A. J.; Lindsay, A. P.; Jayaraman, A.; Lodge, T. P.; Mahanthappa, M. K.; Bates, F. S. Quasicrystals and Their Approximants in a Crystalline-Amorphous Diblock Copolymer. *Macromolecules* 2021, 54 (6), 2647–2660. https://doi.org/10.1021/acs.macromol.0c02871.
- (119) Grzetic, D. J.; Delaney, K. T.; Fredrickson, G. H. Electrostatic Manipulation of Phase Behavior in Immiscible Charged Polymer Blends. *Macromolecules* 2021, 54 (6), 2604–2616. https://doi.org/10.1021/acs.macromol.1c00095.
- (120) Kumar, R.; Fredrickson, G. H. Theory of Polyzwitterion Conformations. *J. Chem. Phys.* **2009**, *131*(10), 104901. https://doi.org/10.1063/1.3216107.
- (121) Sing, C. E.; Zwanikken, J. W.; De La Cruz, M. O. Theory of Melt Polyelectrolyte Blends and Block Copolymers: Phase Behavior, Surface Tension, and Microphase Periodicity. *J. Chem. Phys.* 2015, 142 (3), 34902. https://doi.org/10.1063/1.4905830.
- (122) Ding, S.-P.; Zhang, Z.-K.; Ye, Z.; Du, B.-Y.; Xu, J.-T. Fabrication of High χ-Low N Block Copolymers with Thermally Stable Sub-5 Nm Microdomains Using Polyzwitterion as a Constituent Block. ACS Macro Lett. 2021, 10 (10), 1321–1325. https://doi.org/10.1021/acsmacrolett.1c00461.
- (123) Reddy, A.; Buckley, M. B.; Arora, A.; Bates, F. S.; Dorfman, K. D.; Grason, G. M. Stable Frank-Kasper Phases of Self-Assembled, Soft Matter Spheres. *Proc. Natl. Acad. Sci. U. S. A.* 2018, 115 (41), 10233–10238. https://doi.org/10.1073/pnas.1809655115.
- (124) Zhou, D.; Xu, M.; Ma, Z.; Gan, Z.; Tan, R.; Wang, S.; Zhang, Z.; Dong, X. H. Precisely Encoding Geometric Features into Discrete Linear Polymer Chains for Robust Structural Engineering. *J. Am. Chem. Soc.* **2021**, *143* (44), 18744–18754. https://doi.org/10.1021/jacs.1c09575.
- (125) Schönhals, A.; Kremer, F. Analysis of Dielectric Spectra. In *Broadband Dielectric Spectroscopy*;

- Kremer, F., Schönhals, A., Eds.; Springer Berlin Heidelberg: Berlin, Heidelberg, 2003; Vol. 46, pp 59–98. https://doi.org/10.1007/978-3-642-56120-7 3.
- (126) Wübbenhorst, M.; Van Turnhout, J. Analysis of Complex Dielectric Spectra. I: One-Dimensional Derivative Techniques and Three-Dimensional Modelling. *J. Non. Cryst. Solids* **2002**, *305* (1–3), 40–49. https://doi.org/10.1016/S0022-3093(02)01086-4.
- (127) Havriliak, S.; Negami, S. A Complex Plane Analysis of α-Dispersions in Some Polymer Systems.
  J. Polym. Sci. Part C Polym. Symp. 1966, 14 (1), 99–117.
  https://doi.org/10.1002/polc.5070140111.
- (128) Mei, W.; Han, A.; Hickey, R. J.; Colby, R. H. Effect of Chemical Substituents Attached to the Zwitterion Cation on Dielectric Constant. *J. Chem. Phys.* 2021, 155 (24), 244505. https://doi.org/10.1063/5.0074100.
- (129) Scott, P. J.; Spiering, G. A.; Wang, Y.; Seibers, Z. D.; Moore, R. B.; Kumar, R.; Lokitz, B. S.; Long, T. E. Phosphonium-Based Polyzwitterions: Influence of Ionic Structure and Association on Mechanical Properties. *Macromolecules* 2020, *53* (24), 11009–11018. https://doi.org/10.1021/acs.macromol.0c02166.